Numerical Simulation of the Whole Three-Dimensional Flow in a Stirred Tank with Anisotropic Algebraic Stress Model*

SUN Haiyan(孙海燕) WANG Weijing(王卫京) and MAO Zaisha(毛在砂)**
Institute of Process Engineering (formerly Institute of Chemical Metallurgy), Chinese Academy of Sciences, Beijing 100080, China

Abstract In accordance to the anisotropic feature of turbulent flow, an anisotropic algebraic stress model is adopted to predict the turbulent flow field and turbulent characteristics generated by a Rushton disc turbine with the improved inner-outer iterative procedure. The predicted turbulent flow is compared with experimental data and the simulation by the standard k-ε turbulence model. The anisotropic algebraic stress model is found to give better prediction than the standard k-ε turbulence model. The predicted turbulent flow field is in accordance to experimental data and the trend of the turbulence intensity can be effectively reflected in the simulation. The distribution of turbulent shear rate in the stirred tanks was simulated with the established numerical procedure.
Keywords agitated vessel, anisotropic algebraic stress model, numerical simulation, inner-outer iteration, Rushton turbine

1 INTRODUCTION

Agitated vessels are widely used in the chemical, pharmaceutical and petroleum refinery industries for mixing and chemical reactions. The description of turbulent flow is required for the solution of transport equations modeling the energy and mass transfer in agitated vessels. Also, the knowledge of flow patterns and shear rates from the fluid dynamic prediction is very valuable for the design purpose. To solve the time-averaged equations of the turbulent flow field in an agitated vessel, a turbulence model is required for the evaluation of Reynolds stress terms. The most widely used turbulence model is the standard k-ε turbulence model, which is based on the Boussinesq hypothesis of eddy viscosity. When the Reynolds stress terms are solved from Reynolds stress transport equations, the Reynolds stress model (RSM) is established. The algebraic stress model (ASM) is the approximate form of RSM in which the Reynolds stress terms are given in the form of algebraic equations.

In agitated vessels, apart from anisotropy of turbulence generation due to the strong rotational nature, the flow is periodic due to the fact that the impeller blades sweep past the baffles. van't Riet *et al.*[1] pointed out that this resulted in periodic velocity fluctuations, a phenomenon called pseudo-turbulence. Turbulent intensity is usually strong in a dominant direction and weaker in other directions. In the numerical research of agitated vessels, many researchers[2−5] used isotropic turbulence models, mostly the standard k-ε turbulence model. In order to account for the anisotropy of turbulence in the flow field, the anisotropic turbulence model is desired. Though the Reynolds stress model is intrinsically anisotropic, it is too complicated for engineering applications. Besides, unsuitable initial conditions often lead to negative values for turbulent energy and failure of simulation[6]. As a result, a compromise algebraic stress model (ASM) was developed by Rodi[7]. ASM has been applied successfully in many near parallel flows, in which the ASM formulation can usually be simplified such that the Reynolds stresses are nearly explicitly related to the mean velocity field. In the case of general two- or three-dimensional flow, such as the complicated flow in the agitated vessel, a set of algebraic equations is to be solved directly for the stresses. This is usually carried out numerically at each time step or iteration in the overall solution procedure. Since there is no diffusion or damping in the ASM equation set, it is very difficult to maintain numerical solution stable. Very small time steps or very small (under-)relaxation factors are necessary to obtain a convergent solution. The amount of computational effort is thus increased to the point that the advantage of simplicity of the ASM model is lost. For the remedy, an explicit form of the stress-strain relation was required. Pope[8] was the first to propose a methodology to obtain an explicit relation for the Reynolds stress tensor from the implicit algebraic stress model that Rodi[7] developed. The methodology leading to explicit algebraic stress

---

models is based on the technique of linear algebra. Owing to the complexity of the algebra, Pope was only able to obtain a solution for two-dimensional turbulent flows. After that, some researchers[9−13] extended the results of Pope to three-dimensional turbulence flows.

Numerical simulation of unsteady flow in the impeller region in an agitated vessel is another challenge. The most direct approach is to solve the time-dependent fluid mechanic equations, but it demands a great deal of computer memory and time. The second method is the "black box" method in which the impeller region is not explicitly simulated and its effects are represented by suitable, empirically derived boundary conditions imposed on the external flow. The main limitation of this approach is that it lacks the generality: experimental data, including turbulence quantities, are needed for each specific case under investigation, while such data are available only for a few vessel and impeller shape. For example, Hou et al.[14] used this method to simulate the flow field under different operating conditions. In order to overcome the expensive demand for experimental data, some new computational procedure has been proposed, such as the "snapshot" approach by Ranade and Doment[15] which was in fact an approximate treatment. Based on the successful experience of the "black box" model, Brucato et al.[16] proposed the inner-outer iteration method which did not require experimental measurements. The weakness of this method was that the information exchanged between the inner and outer domains was averaged over the azimuthal direction during iterations. As a result, some important flow features, such as the periodic pseudo-turbulence was lost. Wang and Mao[17] improved the "inner-outer" iteration method, in which

the boundary information was not averaged over the azimuthal direction so as to preserve the periodic pseudo-turbulence characteristics, and good prediction of velocity components in tangential and axial direction was demonstrated by this method using the isotropic standard k-ε turbulence model.

Nobody used the RSM to simulate the three-dimensional turbulent flow in agitated vessels to date, and only Bakker and van den Akker[18] used the ASM to model the Reynolds stresses by the "black box" model with the experimental data as the boundary conditions of the impeller region. The main purpose of this paper is to use the three-dimensional explicit algebraic stress model of Gatski and Speziale[11] to predict the turbulent flow in terms of velocity components, turbulent intensity, kinetic energy k and dissipation rate ε generated by a Rushton disc turbine with the improved inner-outer iterative method.

2 FLUID FLOW MODEL
2.1 Governing equations

The current form of averaged steady-state Navier-Stokes equation, continuity equation, turbulent kinetic energy k and turbulence dissipation ε equations in the cylindrical coordinate system can be written as

$$
\frac{1}{r}\frac{\partial}{\partial r}(\rho r\phi V_r) + \frac{1}{r}\frac{\partial}{\partial \theta}(\rho\phi V_\theta) + \frac{\partial}{\partial z}(\rho\phi V_z)
$$
$$
= \frac{1}{r}\frac{\partial}{\partial r}\left(\Gamma_\phi r\frac{\partial\phi}{\partial r}\right) + \frac{1}{r}\frac{\partial}{\partial\theta}\left(\frac{\Gamma_\phi}{r}\frac{\partial\phi}{\partial\theta}\right) +
$$
$$
\frac{\partial}{\partial z}\left(\Gamma_\phi\frac{\partial\phi}{\partial z}\right) + S_\phi \tag{1}
$$

where ϕ denotes the general parameter, Γ_ϕ denotes the diffusion coefficient of ϕ, S_ϕ the source term in the equation, as detailed in Table 1.

Table 1 Diffusion coefficient and source terms in transport equations

ϕ	Γ_ϕ	S_ϕ
1	0	0
V_r	μ	$-\dfrac{\partial p}{\partial r} + \rho\dfrac{V_\theta^2}{r} - \dfrac{2\mu}{r^2}\dfrac{\partial V_\theta}{\partial\theta} - \dfrac{\mu V_r}{r^2} + \rho\dfrac{\overline{v_\theta v_\theta}}{r}$
		$-\dfrac{1}{r}\dfrac{\partial}{\partial r}(r\rho\overline{v_r v_r}) - \dfrac{1}{r}\dfrac{\partial}{\partial\theta}(\rho\overline{v_r v_\theta}) - \dfrac{\partial}{\partial z}(\rho\overline{v_r v_z}) + F_r$
V_θ	μ	$-\dfrac{1}{r}\dfrac{\partial p}{\partial\theta} - \rho\dfrac{V_\theta V_r}{r} + \dfrac{2\mu}{r^2}\dfrac{\partial V_r}{\partial\theta} - \mu\dfrac{V_\theta}{r^2} - \rho\dfrac{\overline{v_r v_\theta}}{r}$
		$-\dfrac{1}{r}\dfrac{\partial}{\partial r}(r\rho\overline{v_r v_\theta}) - \dfrac{1}{r}\dfrac{\partial}{\partial\theta}(\rho\overline{v_\theta v_\theta}) - \dfrac{\partial}{\partial z}(\rho\overline{v_\theta v_z}) + F_\theta$
V_z	μ	$-\dfrac{\partial p}{\partial z} + \rho g - \dfrac{1}{r}\dfrac{\partial}{\partial r}(r\rho\overline{v_z v_r}) - \dfrac{1}{r}\dfrac{\partial}{\partial\theta}(\rho\overline{v_z v_\theta}) - \dfrac{\partial}{\partial z}(\rho\overline{v_z v_z})$
k	μ_t/σ_k	$G - \rho\varepsilon$
ε	μ_t/σ_ε	$\dfrac{\varepsilon}{k}(C_{\varepsilon 1}G - C_{\varepsilon 2}\rho\varepsilon)$

In Table 1, G is defined by

$$G = -\rho\overline{v_r v_r}\frac{\partial V_r}{\partial r} - \rho\overline{v_\theta v_\theta}\left(\frac{1}{r}\frac{\partial V_\theta}{\partial \theta} + \frac{V_r}{r}\right) - \rho\overline{v_z v_z}\frac{\partial V_z}{\partial z} -$$
$$\rho\overline{v_r v_\theta}\left[r\frac{\partial}{\partial r}\left(\frac{V_\theta}{r}\right) + \frac{1}{r}\frac{\partial V_r}{\partial \theta}\right] -$$
$$\rho\overline{v_\theta v_z}\left(\frac{\partial V_\theta}{\partial z} + \frac{1}{r}\frac{\partial V_z}{\partial \theta}\right) - \rho\overline{v_r v_z}\left(\frac{\partial V_z}{\partial r} + \frac{\partial V_r}{\partial z}\right) \quad (2)$$

and μ_t is defined as

$$\mu_t = \nu_t\rho = C_\mu\rho\frac{k^2}{\varepsilon} \quad (3)$$

F_r, F_θ[16] are the body forces including both centrifugal and Coriolis terms, which arise only when a rotating reference frame (non-inertial frame) is used

$$F_r = \rho r\omega^2 + 2\rho\omega V_\theta, \quad F_\theta = -2\rho\omega V_r \quad (4)$$

while in the inertial frame

$$F_r = 0, \quad F_\theta = 0 \quad (5)$$

The reference values of the model constants are[19]

$$C_\mu = 0.09, \quad C_{\varepsilon 1} = 1.44, \quad C_{\varepsilon 2} = 1.92,$$
$$\sigma_k = 1.0, \quad \sigma_\varepsilon = 1.3 \quad (6)$$

The stress tensor of incompressible fluid in the inertial frame are[11]

$$\overline{v_i v_j} = \frac{2}{3}k\delta_{ij} - 2C_\mu^*\frac{k^2}{\varepsilon}\overline{S}_{ij} -$$
$$\beta_1\frac{k^3}{\varepsilon^2}\left(\overline{S}_{im}\overline{\omega}_{mj} + \overline{S}_{jm}\overline{\omega}_{mi}\right) +$$
$$\beta_2\frac{k^3}{\varepsilon^2}\left(\overline{S}_{im}\overline{S}_{mj} - \frac{1}{3}\overline{S}_{mn}\overline{S}_{mn}\delta_{ij}\right) +$$
$$\beta_3\frac{k^3}{\varepsilon^2}\left(\overline{\omega}_{im}\overline{\omega}_{mj} - \frac{1}{3}\overline{\omega}_{mn}\overline{\omega}_{mn}\delta_{ij}\right) \quad (7)$$

The stress tensor of the incompressible fluid in the non-inertial frame are[11]

$$\overline{v_i v_j} = \frac{2}{3}k\delta_{ij} - 2C_\mu^*\frac{k^2}{\varepsilon}\overline{S}_{ij} -$$
$$\beta_1\frac{k^3}{\varepsilon^2}\left(\overline{S}_{im}\overline{W}_{mj} + \overline{S}_{jm}\overline{W}_{mi}\right) +$$
$$\beta_2\frac{k^3}{\varepsilon^2}\left(\overline{S}_{im}\overline{S}_{mj} - \frac{1}{3}\overline{S}_{mn}\overline{S}_{mn}\delta_{ij}\right) +$$
$$\beta_3\frac{k^3}{\varepsilon^2}\left(\overline{W}_{im}\overline{W}_{mj} - \frac{1}{3}\overline{W}_{mn}\overline{W}_{mn}\delta_{ij}\right) \quad (8)$$

with

$$\overline{W}_{ij} = \overline{\omega}_{ij} + \varepsilon_{mji}\Omega_m \quad (9)$$

$$\overline{S}_{\theta\theta} = \left(\frac{1}{r}\frac{\partial V_\theta}{\partial \theta} + \frac{V_r}{r}\right) \quad (10)$$

$$\overline{S}_{rr} = \left(\frac{\partial V_r}{\partial r}\right) \quad (11)$$

$$\overline{S}_{zz} = \left(\frac{\partial V_z}{\partial z}\right) \quad (12)$$

$$\overline{S}_{r\theta} = \overline{S}_{\theta r} = \frac{1}{2}\left[\frac{1}{r}\frac{\partial V_r}{\partial \theta} + r\frac{\partial}{\partial r}\left(\frac{V_\theta}{r}\right)\right] \quad (13)$$

$$\overline{S}_{rz} = \overline{S}_{zr} = \frac{1}{2}\left(\frac{\partial V_z}{\partial r} + \frac{\partial V_r}{\partial z}\right) \quad (14)$$

$$\overline{S}_{\theta z} = \overline{S}_{z\theta} = \frac{1}{2}\left(\frac{\partial V_\theta}{\partial z} + \frac{1}{r}\frac{\partial V_z}{\partial \theta}\right) \quad (15)$$

$$\overline{\omega}_{rr} = \overline{\omega}_{zz} = \overline{\omega}_{\theta\theta} = 0 \quad (16)$$

$$\overline{\omega}_{r\theta} = -\overline{\omega}_{\theta r} = \frac{1}{2}\left[\frac{1}{r}\frac{\partial V_r}{\partial \theta} - r\frac{\partial}{\partial r}\left(\frac{V_\theta}{r}\right)\right] \quad (17)$$

$$\overline{\omega}_{zr} = -\overline{\omega}_{rz} = \frac{1}{2}\left(\frac{\partial V_z}{\partial r} - \frac{\partial V_r}{\partial z}\right) \quad (18)$$

$$\overline{\omega}_{\theta z} = -\overline{\omega}_{z\theta} = \frac{1}{2}\left(\frac{\partial V_\theta}{\partial z} - \frac{1}{r}\frac{\partial V_z}{\partial \theta}\right) \quad (19)$$

The coefficients given in Refs. [10,11] are

$$\frac{G}{\rho\varepsilon} = \frac{C_{\varepsilon 2} - 1}{C_{\varepsilon 1} - 1}, \quad C_1 = 3.4 + 1.8 \times \frac{G}{\rho\varepsilon}, \quad C_2 = 0.8,$$
$$C_3 = 1.25, \quad C_4 = 0.40, \quad g = \left(\frac{1}{2}C_1 + \frac{G}{\rho\varepsilon} - 1\right)^{-1},$$
$$C_\mu^* = \frac{1}{2}g\left(\frac{4}{3} - C_2\right), \quad \beta_1 = \frac{1}{2}g^2\left(2 - C_4\right)\left(\frac{4}{3} - C_2\right),$$
$$\beta_2 = g^2\left(2 - C_3\right)\left(\frac{4}{3} - C_2\right), \quad \beta_3 = -0.02$$

2.2 Boundary conditions

(1) On the symmetry axis ($r=0$),

$$V_r = 0, \quad \frac{\partial \phi}{\partial r} = 0, \quad \phi \neq V_r \quad (20)$$

(2) At free liquid surface ($z=H$),

$$V_z = 0, \quad \frac{\partial \phi}{\partial z} = 0, \quad \phi \neq V_z \quad (21)$$

(3) At the impermeable wall,

$$r = R, \quad \frac{\partial \phi}{\partial r} = 0 \quad (\phi \neq V_r), \quad V_r = 0 \quad (22)$$

2.3 Modification of the model parameters

The k and ε equations in Table 1 is only suitable for the fully turbulent region. In agitated vessels, not only the fully turbulent region, but also the transitional and laminar regions exist, so the expression for

C_μ^*, $C_{\varepsilon 1}$ and $C_{\varepsilon 2}$ should be modified as by Lam and Bremhorst[20]

$$C_\mu^* = \frac{1}{2}g\left(\frac{4}{3} - C_2\right)\left(1 + \frac{20.5}{R_t}\right)[1 - \exp(-0.0165R_k)]^2 \tag{23}$$

$$C_{\varepsilon 1} = 1.44\left[1 + \left(0.05 \times \frac{C_\mu^*}{C_\mu}\right)^3\right] \tag{24}$$

$$C_{\varepsilon 2} = 1.92\left[1.0 - \exp\left(-R_t^2\right)\right] \tag{25}$$

in which two special Reynolds numbers are used

$$R_t = \frac{\rho k^2}{\mu\varepsilon}, \quad R_k = \frac{\rho k^{1/2}y_w}{\mu} \tag{26}$$

This k-ε model with coefficients given by Eqs. (23) to (26) does not require using the wall functions or introducing additional terms in the k and ε equations for the low Reynolds number region. Thus they appear to be particularly suitable for the flow in agitated vessels where the flow is in circulation from the higher velocity impeller stream through the lower velocity region in the rest of the tank.

3 NUMERICAL PROCEDURE

3.1 Computational domains

The whole vessel is subdivided into two partly overlapping zones, as shown in Fig. 1: an "inner" domain encircling the impeller, and an "outer" one including the baffles and reaching the vessel wall and bottom. Firstly, the inner flow field is calculated in the non-inertial frame with arbitrary boundary conditions imposed on the surface Σ1. A first trial flow field is thus obtained in the whole impeller region, including the distributions of velocity, turbulent kinetic energy, turbulence dissipation and Reynolds stresses on the boundary surface Σ2. Secondly, the variables on the surface Σ2 are used as boundary conditions to calculate the outer flow field in the inertial frame. Then, the information of the flow field in the whole vessel is now available, including the information on the boundary surface Σ1. These values are in turn used as boundary conditions for a second iteration simulation of the "inner" domain and so on, until the system attains a satisfactory numerical convergence. Since the two frames are different, the information iteratively exchanged in between should be corrected by the rotation of non-inertial reference frame.
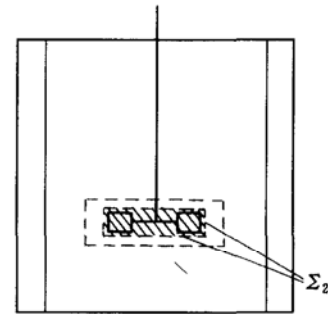
3.2 Computation grids

The control volume formulation with staggered grids is adopted to simulate the turbulent flow. Fig. 2 shows the control volumes and nodes in the r-θ plane and the juxtaposition of nodes on the other planes is analogous. Scalar quantities such as p, k and ε are

evaluated at note P, whereas the momentum in radial, tangential and axial directions are computed at side faces of cell P. For Reynolds stresses, the shear stress component $\tau_{r\theta}$ is evaluated at the left bottom corner of the scalar cell, as done by Pope and Whitelaw[21], whereas the shear stress component τ_{rr} and $\tau_{\theta\theta}$ are evaluated at the same locations as V_r and V_θ respectively. The staggered allocation of variables is more advantageous to evaluating the terms of shear stress and shear strain combinations than evaluating these at the same node P.
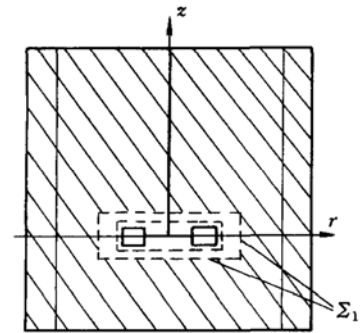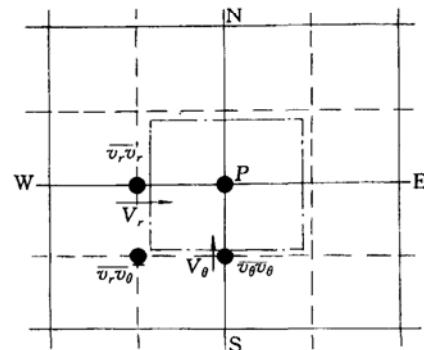

(a) Inner domain

(b) Outer domain

Figure 1 Inner and outer calculation domains
(Shaded area is excluded from the computation; Σ1 and Σ2 are control volume layers on which boundary conditions are iteratively imposed)

Figure 2 Juxtaposition of grid nodes in r-θ plane
● grid node; ----- control cell of node P

The discretization of equations is performed by using the power law scheme[22] and the pressure is solved

by the SIMPLE algorithm[22]. To check the possible grid dependency, several grids were tested: $30 \times 24 \times 60$, $30 \times 36 \times 60$, $36 \times 24 \times 60$, $36 \times 36 \times 60$, $36 \times 48 \times 60$, $36 \times 48 \times 75$, $36 \times 48 \times 90$ [numbers of nodes in (r, θ, z) coordinates]. The velocity components V_r and V_θ at the first node near the impeller tip with $z=0$ simulated with different grids are shown in Table 2. It can be seen that the calculation results change little as the grid was increased to $36 \times 48 \times 90$. So the $36 \times 48 \times 90$ grid is chosen for all subsequent simulations.

Table 2   Radial and tangential velocities near impeller tip simulated with different grids

Grid size	V_r/V_{tip}	V_θ/V_{tip}
$30 \times 24 \times 60$	0.393	0.369
$30 \times 36 \times 60$	0.410	0.368
$36 \times 24 \times 60$	0.432	0.400
$36 \times 36 \times 60$	0.446	0.397
$36 \times 48 \times 60$	0.452	0.394
$36 \times 48 \times 75$	0.485	0.408
$36 \times 48 \times 90$	0.490	0.414

3.3 Numerical procedure

Using the explicit ASM expressions in Eqs. (7) and (8), the Reynolds stress terms in radial, tangential, axial momentum equations are rearranged and expressed in the conventional form with convection, diffusion and source terms as in Eq. (1). As the molecular viscosity in the diffusion term is small, this may induce numerical instability during iterations. Therefore, a pseudo-gradient diffusion term is added, and in the mean time an equal negative source is put in the source term to balance it. For the pseudo-gradient diffusion terms, isotropic eddy viscosity $\nu_t = C_\mu k^2/\varepsilon$ is used.

From the numerical point of view, convergence of these transport equations would be difficult due to their strong nonlinearity. In fact, the chance of convergence is minimal when the computation starts with an arbitrary guessed Reynolds stress field. For this reason a two-step procedure is used. Firstly, the general momentum equations are solved along with the conventional standard k-ε turbulence model with

$$\overline{v_r v_r} = \frac{2}{3}k - 2\nu_t \overline{S}_{rr}, \quad \overline{v_\theta v_\theta} = \frac{2}{3}k - 2\nu_t \overline{S}_{\theta\theta},$$

$$\overline{v_z v_z} = \frac{2}{3}k - 2\nu_t \overline{S}_{zz}, \quad \overline{v_r v_\theta} = -2\nu_t \overline{S}_{r\theta},$$

$$\overline{v_r v_\theta} = -2\nu_t \overline{S}_{rz}, \quad \overline{v_\theta v_z} = -2\nu_t \overline{S}_{\theta z}$$

After about 2000 iterations, the Reynolds stresses based on Eqs. (7) and (8) are invoked. When the relative residual of each equation is below 10^{-4}, the computation is considered as convergent.

4 RESULTS AND DISCUSSION

Several sets of experimental data from the literature are compared with our numerical simulation.

First the flow field which was measured by Wu and Patterson[23] with laser-Doppler-velocimeter(LDV) is simulated. The experimental apparatus used by them consists of a baffled stirred tank with a standard six-blade disk turbine. A schematic diagram of the tank and impeller, and the coordinates used for the presentation of the results are shown in Fig. 3. Four wall baffles were one-tenth of the tank diameter wide. The tank was filled with water and the impeller speed used was 200 r·min^{-1}.
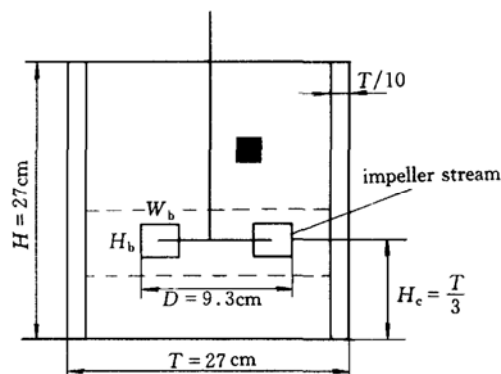
Figure 3   The dimensions of stirred tank and impeller

4.1 Velocity component prediction

The flow fields calculated on a three-dimensional grid ($36 \times 48 \times 90$) in the r-z plane and in the r-θ planes are shown in Fig. 4. The stream is discharged radially from the impeller, then part of the stream is bent up, and the rest flows down along the tank wall. The flow returns finally to the impeller, giving a picture in accord to our physical intuition. Beside two large vortexes below and above the impeller stream roughly at $r = 0.7R$, two small vortexes are recognized appearing near the upper and lower corner beside the blade tip. This is consistent with the trailing vortices described by van't Riet et al.[1], who found that a pair of vortices originated from behind each blade rolled out into the impeller stream with strong but opposite directions of rotation around their axes, which were nearly perpendicular to the blade.

4.2 Turbulence kinetic energy and dissipation

Typical results for the turbulence kinetic energy and its dissipation rates on the 45° r-z plane are given in Figs. 5 and 6. The contours of turbulence kinetic energy at the impeller tip is more densely distributed than that in the region away from the impeller. This phenomenon can also be seen from the contours for the dissipation rates of turbulence kinetic energy in Fig. 6. Most of the turbulent energy dissipation occurs in the impeller stream. This means that the turbulence energy is consumed quickly in the impeller

stream. In the rest of the agitated vessel, the dissipation rates of turbulence kinetic energy are relatively small. Based on the experiment data, Wu and Patterson[23] quantified from energy dissipation and concluded that about 60% of the total turbulent kinetic energy was dissipated in the impeller region and in the impeller stream. The calculated result in this paper according to ε is the same: the energy dissipated in these regions is 65.7% of the total energy.
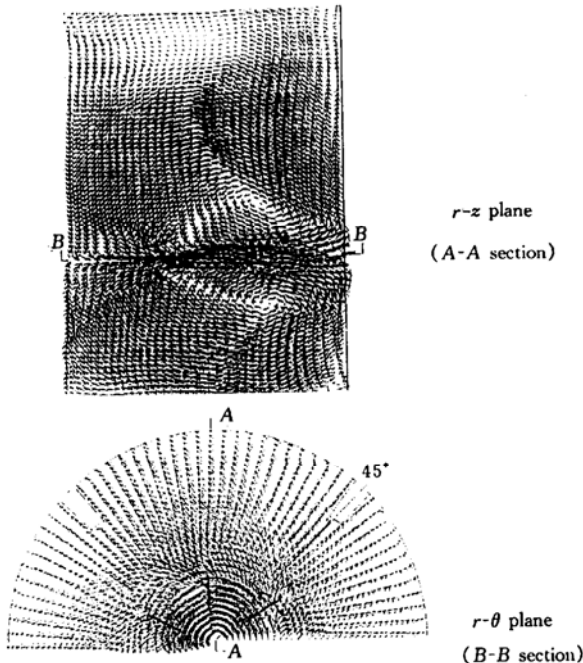

Figure 6   Contour map of ε on the 45° r-z plane

r-z plane

(A-A section)

r-θ plane

(B-B section)

Figure 4   Velocity fields in the agitated vessel

Figure 7   Mean radial velocity profiles
near impeller tip
($N = 200\,\mathrm{r\cdot min^{-1}}$, $T = H = 0.27\,\mathrm{m}$, $D = 0.093\,\mathrm{m}$,
$H_c = H/3$, $r = 6\,\mathrm{cm}$;
standard six blade Rushton turbine, $H_b = D/5$, $W_b = D/4$)
● exp. data, Wu & Patterson[23];
- - - - standard k-ε turbulence model;
—— algebraic stress model
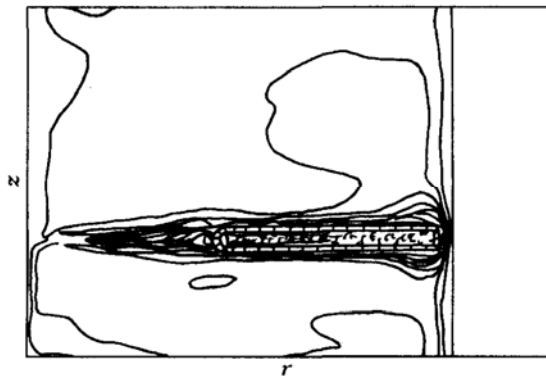
Figure 5   Contour map of k on the 45° r-z plane

4.3 Mean velocity components

4.3.1 At the impeller tip

The comparison of the values of velocity components calculated by standard k-ε turbulence model, the values calculated by the ASM and the experimental data by LDV[23] near the impeller tip are shown in Figs. 7, 8 and 9. The origin of the axial coordinate
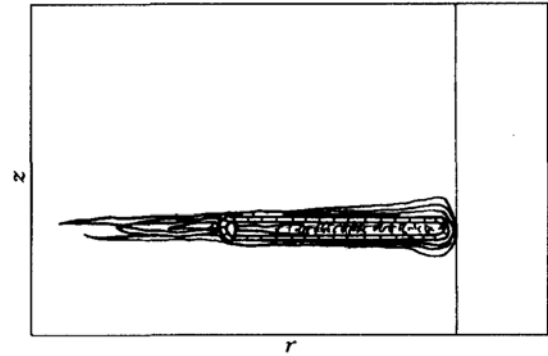
is on the center plane of the impeller. The velocities are normalized with the impeller tip velocity. As the velocities in the impeller tip measured experimentally were periodically averaged and the calculated values are instantaneous, the calculated values should be averaged by the "spatial average method" of Harvey and Rogers[24] for the comparison. It can be seen from the Figs. 7, 8 and 9 that the ASM model can give better prediction than the standard k-ε turbulence model.

4.3.2 Impeller stream

Comparisons of the tangential and radial velocity components in the impeller stream predicted using the two turbulence models are made with literature data in Figs. 10, 11 and 12 respectively. Fig. 10 shows the normalized tangential velocities on the impeller plane as a function of radial position. The experimental data were measured by a laser velocimeter[25]. In Figs. 11 and 12, the normalized radial and tangential velocities in the impeller stream predicted by these two models are compared with the experimental data taken by Cutter[26] with the photographic method.
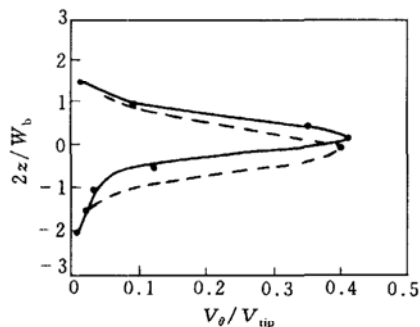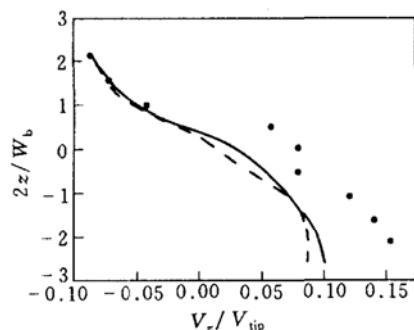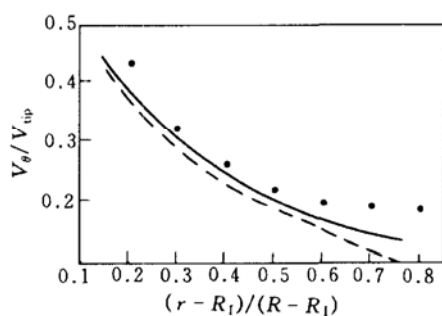
Figure 8   Mean tangential velocity profiles near impeller tip
($N = 200\,\text{r·min}^{-1}$, $T = H = 0.27\,\text{m}$, $D = 0.093\,\text{m}$,
$H_\text{c} = H/3$, $r = 6\,\text{cm}$;
standard six blade Rushton turbine, $H_\text{b} = D/5$, $W_\text{b} = D/4$)
● exp. data, Wu & Patterson[23];
- - - - standard k-ε turbulence model;
—— algebraic stress model

Figure 9   Mean axial velocity profiles near impeller tip
($N = 200\,\text{r·min}^{-1}$, $T = H = 0.27\,\text{m}$, $D = 0.093\,\text{m}$,
$H_\text{c} = H/3$, $r = 6\,\text{cm}$;
standard six blade Rushton turbine, $H_\text{b} = D/5$, $W_\text{b} = D/4$)
● exp. data, Wu & Patterson[23];
- - - - standard k-ε turbulence model;
—— algebraic stress model

Figure 10   Radial profiles of mean tanential velocity in the impeller stream
($N = 200\,\text{r·min}^{-1}$, $T = 0.089\,\text{m}$, $H = 0.1143\,\text{m}$,
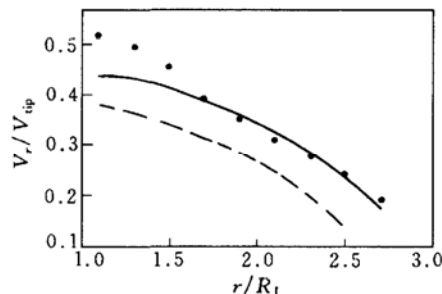$D = 0.0304\,\text{m}$, $H_\text{c} = H/2$, $z = 0$;
standard six blade Rushton turbine, $H_\text{b} = D/5$, $W_\text{b} = D/4$)
● exp. data, Chen[25];
- - - - standard k-ε turbulence model;
—— algebraic stress model

4.3.3 Bulk region

In Fig. 13 comparison is made for the axial velocity component as the function of radial position. The experimental data were given by Ranade and Joshi[27] with a laser Doppler anemometer. The comparison indicates that ASM can give better prediction than the standard k-ε turbulence model.
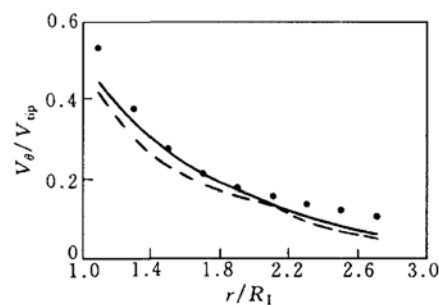

Figure 11   Radial Profiles of mean radial velocity in the impeller stream
($N = 400\,\text{r·min}^{-1}$, $T = 0.2921\,\text{m}$, $H = 0.3048\,\text{m}$,
$D = 0.1016\,\text{m}$, $H_\text{c} = H/3$, $z = 0$;
standard six blade Rushton turbine, $H_\text{b} = D/5$, $W_\text{b} = D/4$)
● exp. data, Cutter[26];
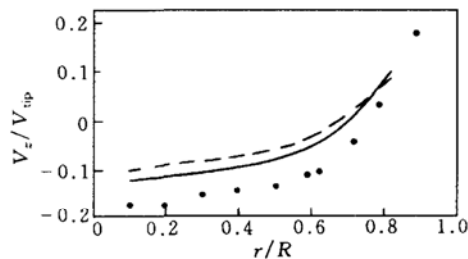- - - - standard k-ε turbulence model;
—— algebraic stress model

Figure 12   Radial profiles of mean tangential velocity in the impeller stream
($N = 400\,\text{r·min}^{-1}$, $T = 0.2921\,\text{m}$, $H = 0.3048\,\text{m}$,
$D = 0.1016\,\text{m}$, $H_\text{c} = H/3$, $z = 0$;
standard six blade Rushton turbine, $H_\text{b} = D/5$, $W_\text{b} = D/4$)
● exp. data, Cutter[26];
- - - - standard k-ε turbulence model;
—— algebraic stress model

Figure 13   Radial profiles of axial velocity in the bulk region of the tank
($N = 200\,\text{r·min}^{-1}$, $T = 0.30\,\text{m}$, $H = 0.30\,\text{m}$,
$D = 0.10\,\text{m}$, $H_\text{c} = H/2$, $z/R = 0.333$;
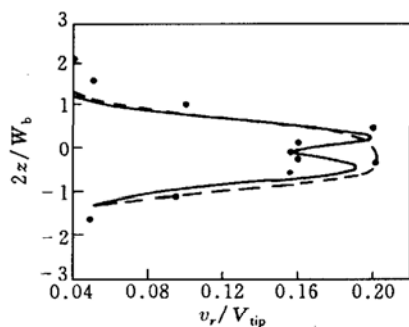standard six blade Rushton turbine, $H_\text{b} = D/5$, $W_\text{b} = D/4$)
● exp. data, Ranade & Joshi[27];
- - - - standard k-ε turbulence model;
—— algebraic stress model
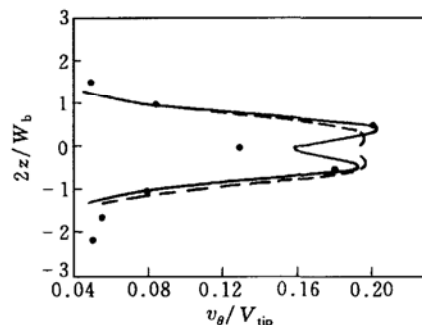
4.4 Turbulent intensity

The profiles of the turbulent intensity near the impeller tip are shown in Figs. 14, 15 and 16. The velocity fluctuations are extracted from the simulated Reynolds stresses expressed in Eq. (8). Since the fluctuations are obtained in the non-inertial coordinate in which the impeller rotates with the reference frame, the pseudo-turbulence component is not included. However, the fluctuation velocities measured experimentally by Wu and Patterson[23] are not the random velocity fluctuation, because the periodic sweeping of impeller-induced vortices over the stationary measuring point is the source of nonrandom periodic fluctuations, Therefore, the periodic velocity fluctuation resulting from the disturbance of impeller vortices should be subtracted from the total turbulence by an autocorrelation method to obtain the random fluctuation velocities[23]. The random fluctuation velocity is the maximum at $2z/W_b = 0.5$ and $2z/W_b = -0.5$ (about half the width of the blade), approximately corresponding to the centers of upper and lower vortices respectively, where the disturbance is the strongest, as depicted by van't Riet et al.[1] It can be seen from Figs. 14—16 that the ASM can more effectively reflected the trend of the turbulent intensity than the standard k-ε turbulence model in the simulation.

To show how far the impeller stream and the trailing vortices can reach and affect the turbulence field, the turbulent intensities at the center plane ($z = 0$) of the stream are plotted as a function of radial position in Fig. 17. Generally, such relative intensities from 0 to 100% are found in the impeller stream. The relative resultant turbulent intensity in the r-θ direction can be defined as
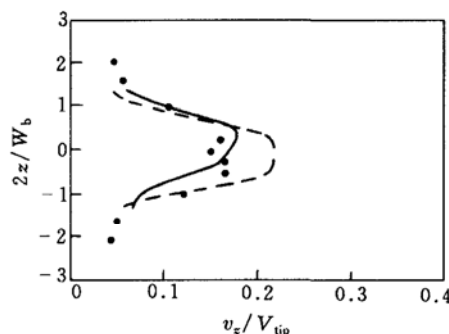

Figure 15   Profiles of tangential turbulence intensity near impeller tip
($N = 200\,\mathrm{r \cdot min^{-1}}$, $T = H = 0.27\,\mathrm{m}$, $D = 0.093\,\mathrm{m}$, $H_c = H/3$, $r = 5\,\mathrm{cm}$; standard six blade Rushton turbine, $H_b = D/5$, $W_b = D/4$)
● exp. data, Wu & Patterson[23];
- - - - standard k-ε turbulence model;
—— algebraic stress model

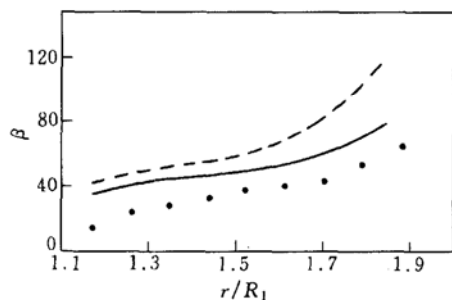Figure 16   Profiles of axial turbulent intensity near impeller tip
($N = 200\,\mathrm{r \cdot min^{-1}}$, $T = H = 0.27\,\mathrm{m}$, $D = 0.093\,\mathrm{m}$, $H_c = H/3$, $r = 5\,\mathrm{cm}$; standard six blade Rushton turbine, $H_b = D/5$, $W_b = D/4$)
● exp. data, Wu & Patterson[23];
- - - - standard k-ε turbulence model;
—— algebraic stress model

$$\beta = \frac{\sqrt{\overline{v_r v_r} + \overline{v_\theta v_\theta}}}{\sqrt{V_r V_r + V_\theta V_\theta}} \qquad (27)$$

The ASM prediction is more close to the experimental data than the standard k-ε mode in magnitude and the trend of variation is more parallel to the data.

In the application of stirred tanks, the shear stress is an important parameter for its close relation to the performance of dispersing, mixing, interphase mass transfer and growth of microbial species. However, there is no effective technique for experimental measurement of shear stress in turbulent single-phase and multiphase flow. In this case, it is beneficial to get useful information of shear stress form numerical simulation. Fig. 18 shows the axial profiles of turbulent shear rate γ at different radial position as the function of axial coordinate z for a case with high agitation speed. Turbulent shear rate is defined tentatively

Figure 14   Profiles of radial turbulent intensity near impeller tip
($N = 200\,\mathrm{r \cdot min^{-1}}$, $T = H = 0.27\,\mathrm{m}$, $D = 0.093\,\mathrm{m}$, $H_c = H/3$, $r = 5\,\mathrm{cm}$; standard six blade Rushton turbine, $H_b = D/5$, $W_b = D/4$)
● exp. data, Wu & Patterson[23];
- - - - standard k-ε turbulence model;
—— algebraic stress model

Figure 17   Radial distribution of relative resultant turbulent intensity at the center plane of the impeller stream
($N = 600$ r·min^{-1}, $T = H = 0.457$ m, $D = 0.228$ m, $H_c = H/2$, $z = 0$;
standard six blade Rushton turbine, $H_b = D/5$, $W_b = D/4$)
● exp. data[28];
- - - - standard k-ε turbulence model;
——— algebraic stress model
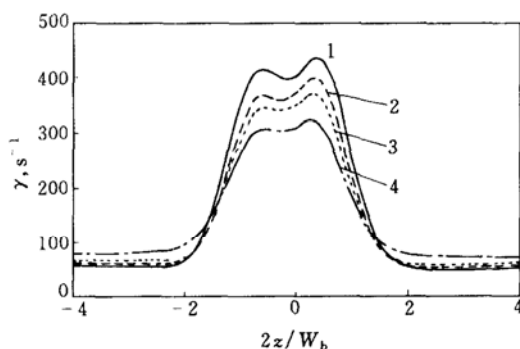
Figure 18   Turbulent shear rate on the Kolmogoroff length scale at different radial positions
($N = 600$ min^{-1}, $T = H = 0.457$ m, $D = 0.228$ m, $H_c = H/2$;
standard six blade Rushton turbine, $H_b = D/5$, $W_b = D/4$)
r/R_I: 1—1.17; 2—1.24; 3—1.30; 4—1.43

as the ratio of the turbulent intensity to the local Kolmogoroff length

$$\gamma = \frac{\sqrt{(\overline{v_r v_r} + \overline{v_\theta v_\theta} + \overline{v_z v_z})}}{L} \quad (28)$$

where the local Kolmogoroff length scale is[29]

$$L = \left(\frac{\nu_t^3}{\varepsilon}\right)^{\frac{1}{4}} \quad (29)$$

in accordance to the general theory of turbulence model[29]. It indicates that the highest shear rate up to 450 s^{-1} is in the impeller region at the blade tips, which is almost an order of magnitude higher than that in the bulk region. When a biochemical process with significant shear sensitivity is carried out in a stirred tank, this region of extremely high rate of shear should be taken into consideration. This phenomenon can also be seen from the contours of shear rate on the r-z plane shown in Fig. 19 for a smaller tank at lower agitation speed. The contour lines with

10, 20, 40, 80 and 120 s^{-1} are plotted. Again the region with high shear rate is the impeller stream and γ decays gradually along the path as the liquid is circulated back into the regions above and below the disk turbine. Another region with high shear rate is the immediate neighborhood of the turbine disk.

5 CONCLUSIONS

In accordance to the anisotropic feature of turbulent flow in agitated vessels, an anisotropic algebraic stress model is used to predict the turbulent flow field generated by a Rushton disc turbine with the improved inner-outer iterative procedure. Comparison of the prediction by the ASM turbulence model is made with experimental data and the simulation with the standard k-ε turbulence model. It is concluded that the anisotropic algebraic stress model performs better in prediction of the features of turbulent flow in stirred tanks than the standard k-ε turbulence model. Thus predicted turbulent flow field is in accordance to experimental data and the trend of the turbulence intensity can be effectively reflected in the simulation.
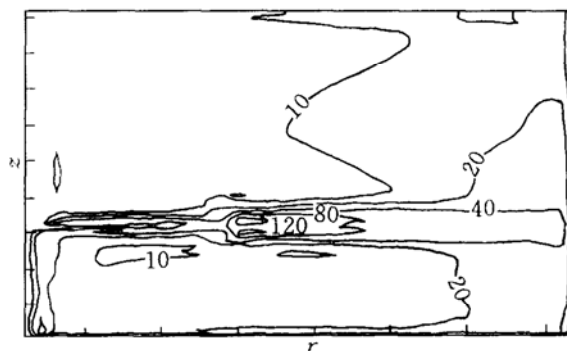
Figure 19   Contour line map of turbulent shear rate on the r-z plane
($N = 200$ r·min^{-1}, $T = H = 0.27$ m, $D = 0.093$ m
standard six blade Rushton turbine, $H_b = D/5$, $W_b = D/4$)

NOMENCLATURE

C_1, C_2, C_3, C_μ^*	parameters in ASM
C_k, C_ε, $C_{\varepsilon 1}$, $C_{\varepsilon 2}$, C_μ	parameters in k-ε model
D	diameter of impeller, m
F_r	centrifugal force, N·m^{-3}
F_θ	Coriolis force, N·m^{-3}
G	generation term of turbulence kinetic energy, kg·m^{-1}·s^{-3}
g	acceleration due to gravity, m·s^{-2}

H	height of liquid, m
H_b	height of blade, m
H_c	clearance, m
k	turbulence kinetic energy, $m^2 \cdot s^{-2}$
N	agitation speed, $r \cdot min^{-1}$
p	pressure, Pa
R	tank radius, m
R_I	impeller radius, m
Re	Reynolds number
r	radial coordinate, m
S_ϕ	source of equation
T	diameter of tank, m
V	mean velocity , $m \cdot s^{-1}$
V_{tip}	velocity of impeller tip, $m \cdot s^{-1}$
v	turbulent fluctuation velocity , $m \cdot s^{-1}$
W_b	width of blade, m
y_w	distance to the wall, m
z	axial coordinate, m
β	turbulent intensity in Eq. (27)
$\beta_1, \beta_2, \beta_3$	parameters in ASM
Γ	diffusion coefficient of turbulence, $Pa \cdot s$
γ	turbulent shear rate defined in Eq. (28), s^{-1}
δ_{ij}	Kronecker denotation
ε	turbulence dissipation energy, $m^2 \cdot s^{-3}$
ε_{mji}	interlaced unit tensor
θ	tangential coordinate, rad
μ	molecule viscosity, $Pa \cdot s$
ν	kinetic viscosity, $m^2 \cdot s^{-1}$
ρ	density, $kg \cdot m^{-3}$
$\sigma_k, \sigma_\varepsilon$	parameters in $k-\varepsilon$ model
τ	Reynolds stress, Pa
ϕ	general variable
Ω	anguler velocity, $rad \cdot s^{-1}$

Subscripts

ij	$rr, zz, rz, r\theta, \theta\theta, z\theta$
r	radial
t	tubulence
z	axial
θ	tangential

REFERENCES

1 van't Riet, K., Bruijn, W., Smith, J. M., "Real and pseudo-turbulence in the discharge stream from a Rushton turbine", *Chem. Eng. Sci.*, **31** (6), 407—412 (1976).

2 Harvey, P. S., Greaves, M., "Turbulent flow in an agitated vessel. Part I: Predictive model", *Chem. Eng. Res. Des.*, **60** (4), 195—200 (1982).

3 Middleton, J. C., Piece, F., Lynch, P. M., "Computations of flow fields and complex reaction yield in turbulent stirred reactors, and comparison with experimental data", *Chem. Eng. Res. Des.*, **64** (1), 19—22 (1986).

4 Ranade, V. V., Joshi, J. R., "Flow Generated by a disc turbine. Part II: Mathematical modeling and comparison with experimental data", *Chem. Eng. Res. Des.*, **68** (1), 34—50 (1990).

5 Fokema, M. D., Kresta, S. M., Wood, P. E., "Important of using the correct impeller boundary for CFD simulations of stirred tanks, conditions", *Can. J. Chem. Eng.*, **72** (2), 177—183 (1994).

6 Zhou, L. X., Numerical Modeling of Turbulent Two-phase Flows and Combustion, Tsinghua University Press, Beijing, 9—79 (1989). (in Chinese)

7 Rodi, W., "A new algebraic relation for calculating the Reynolds stresses", *ZAMM*, **56** (3), 219—221 (1976).

8 Pope, S. B, "A more general effective-viscosity hypothesis", *J. Fluid Mech.*, **72** (11), 331—340 (1975).

9 Yoshizawa, A., "Statistical analysis of the deviation of the Reynolds stress from its eddy-viscosity representation", *Phys. Fluids*, **27** (6), 1377—1387 (1984).

10 Speziale, C. G., "On nonlinear $k-l$ and $k-\varepsilon$ models of turbulence", *J. Fluid Mech.*, **178** (5), 459—475 (1987).

11 Gatski, T. B., Speziale, C. G., "On explicit algebraic stress models for complex turbulent flows", *J. Fluid Mech.*, **254**, 59—78 (1993).

12 Rubinstein, R., Barton, J. M., "Nonlinear Reynolds stress models and the renormalization group", *Phys. Fluids A*, **2** (8), 1472—1476 (1990).

13 Taulbee, D. B., "An improved algebraic Reynolds stress model and corresponding nonlinear stress model", *Phys. Fluids A*, **4** (11), 2555—2561 (1992).

14 Hou, Sh. D., Zhang, Zh., Wang, Y. Ch., Shi, L. T., "Numerical simulation of turbulent flow In stirred tank agitated by axial impeller", *J. Chem. Ind. Eng. (China)*, **51** (1), 70—76 (2000). (in Chinese)

15 Ranade, V. V., Doment, S. M. S., "Computational snap-shot of flow generated by axial impellers in baffled stirred vessels", *Chem. Eng. Res. Des. (Part A)*, **74** (4), 476—484 (1996).

16 Brucato, A., Ciofalo, M., Grisafi, F., Micale, G., "Numerical prediction of flow fields in baffled stirred vessels: A comparison of alternative modeling approached", *Chem. Eng. Sci.*, **53** (21), 3653—3684 (1998).

17 Wang, W. J., Mao, Z. Sh., "Simulation of the whole flow field in a stirred tank with a Rushton paddle", In: Proceedings of the 10th National Conference on Chemical Engineering (NCCE'2000), Zhengzhou, 271—274 (2000). (in Chinese)

18 Bakker, A., van den Akker, H. E. A., "Single-phase flow in stirred reactors", *Chem. Eng. Res. Des.*, **72** (7), 583—593 (1994).

19 Launder, B. E., Spalding, D. B., Mathematical Models of Turbulence, Academic Press, London (1972).

20 Lam, C. K. G., Bremhorst, K. J., "A modified form of the $k-\varepsilon$ model for predicting wall turbulence", *J. Fluids Eng.*, **103** (9), 456—460 (1981).

21 Pope, S. B., Whitelaw, J. H., "The calculation of near-wake flow", *J. Fluid Mech.*, **73** (1), 9—32 (1976).

22 Patankar, S. V., Numerical Heat Transfer and Fluid Flow, New York, McGraw Hill (1980)

23 Wu, H., Patterson, G. K., "Laser-Doppler measurements of turbulent-flow parameters in a stirred miser", *Chem. Eng. Sci.*, **44** (10), 2207—2221 (1989).

24 Harvey, A. D., Lee, C. K., Rogers, S. E., "Steady-state modeling and experimental measurement of a baffled impeller stirred tank", *AIChE J.*, **41** (10), 2177—2186 (1995).

25 Chen, K. Y., Hajduk, J. C., Johnson, J. W., "Laser-Doppler anemometry in a baffled mixing tank", *Chem. Eng. Commun.*, **72** (1), 141—157 (1988).

26 Cutter, L. A., "Flow and turbulence in a stirred tank", *AIChE J.*, **12** (1), 35—45 (1966).

27 Ranade, V. V., Joshi, J. B., "Flow generated by a disc turbine. Part I: Experimental", *Chem. Eng. Res. Des.*, **68** (1), 19—33 (1990).

28 Günkel, A. A., Weber, M. E., "Flow phenomena in stirred tanks. Part I: The impeller stream", *AIChE J.*, **21** (5), 931—937 (1975).

29 Walter, F., Treor, H. M., Handbook of Turbulence, Volume 1: Fundamentals and Applications, Plenum Press, New York and London (1977).